Biochimica et Biophysica Acta 1860 (2016) 2239–2248

Contents lists available at ScienceDirect

Biochimica et Biophysica Acta

journal homepage: www.elsevier.com/locate/bbagen

Interactions of GFAP with ceftriaxone and phenytoin: SRCD and molecular docking and dynamic simulation

Paolo Ruzza [a,*,1], Rosa Maria Vitale [b,1], Rohanah Hussain [c], Barbara Biondi [a], Pietro Amodeo [b], GianPietro Sechi [d], Giuliano Siligardi [c]

[a] Institute of Biomolecular Chemistry of CNR, Padua Unit, Padua, Italy
[b] Institute of Biomolecular Chemistry of CNR, Pozzuoli, Italy
[c] Diamond Light Source Ltd, Harwell Science and Innovation Campus, Didcot, Oxfordshire OX11 0DE, United Kingdom
[d] Department of Clinical and Experimental Medicine, Medical School, University of Sassari, Sassari, Italy

ARTICLE INFO

Article history:
Received 22 December 2015
Received in revised form 14 April 2016
Accepted 27 April 2016
Available online 28 April 2016

Keywords:
Ceftriaxone
Glial fibrillary acidic protein
Neurodegenerative diseases
Synchrotron radiation circular dichroism spectroscopy

ABSTRACT

Background: GFAP is the major intermediate filament protein in mature astrocytes. Its increased expression and aggregation was firstly associated to Alexander's disease, and successively in different neurological diseases including scrapie, Alzheimer's and Creutzfeld–Jacob diseases. Recently, ceftriaxone a multi-potent β-lactam antibiotic able to overcome the blood–brain barrier, successfully eliminated the cellular toxic effects of misfolded mutated GFAP, similarly to phenytoin sodium, in a cellular model of Alexander's disease and inhibited α-synuclein aggregation protecting PC12 cells from the exposure to 6-hydroxydopamine.
Methods: In this study, synchrotron radiation circular dichroism spectroscopy has been used to obtain structural information about the GFAP-ceftriaxone (phenytoin) interactions, while computational methods allowed the identification of the relevant putative binding site of either ceftriaxone or phenytoin on the dimer structure of GFAP, permitting to rationalize the spectroscopic experimental results.
Results: We found that GFAP exhibited enhanced stability upon the addition of two equivalents of each ligands with ceftriaxone imparting a more spontaneous interactions and a more ordered complex system than phenytoin.
Conclusions: SRCD data and MD models indicate a stronger protective effect of ceftriaxone in neurological disorders characterized by an increased production and polymerization of GFAP.
General significance: This result, in addition to our previous works in which we documented that ceftriaxone interacts with α-synuclein inhibiting its pathological aggregation and that a cyclical treatment with this molecule in a patient with adult-onset Alexander's disease halted, and partly reversed, the progression of neurodegeneration, suggests the possibility of a chaperone-like effect of ceftriaxone on protein involved in specific neurodegenerative diseases.

1. Introduction

Glial fibrillary acidic protein (GFAP) is an intermediate filament (IF) type III protein that, along with microtubules and microfilaments, makes up the cytoskeleton of most eukaryotic cells. In addition to vimentin, nestin and synemin, GFAP is a key component of the astrocyte's cytoskeleton that warrants cell integrity and resilience [1]. To date 6 isoforms have been described from normal human and rodent sources, and its molecular weight ranges from 48 kDa for mouse to 49 kDa for human, 50 kDa for bovine, and 51 kDa for rat [2].

The GFAP sequence can be split into three major domains: the N-terminal head region, the central α-helical rod domain, and the C-terminal tail region. The rod domain is highly conserved among IF proteins. In GFAP, it is composed of 345 amino acid residues, containing long tandem repeats of seven amino acid sequences called "heptad repeats". On the contrary, the size and amino acid sequences of the head and tail regions vary among the different IF proteins. The head domain of porcine GFAP, for example, is a highly basic region of 35-amino-acid residues containing eight arginine residues, which adopts a β-turn structure, while the tail region of approximately 50-amino-acid residues has a globular structure [3,4]. Each of these regions plays a role in the complex assembly process. The rod domain has a crucial role in filament assembly, by facilitating coiling between IF proteins. The head domain regulates the filament assembly and the end-to-end interactions, while the tail domain that is involved in the stabilization of the protofilaments/protofibrils by facilitating lateral interactions, modulates

* Corresponding author at: Institute of Biomolecular Chemistry of CNR, Padua Unit, via F. Marzolo 1, Padua, Italy.
E-mail address: paolo.ruzza@unipd.it (P. Ruzza).
[1] These authors contributed equally to this work.

http://dx.doi.org/10.1016/j.bbagen.2016.04.021

the filament diameter [5]. The first event in IF assembly is the association of protein in parallel and anti-parallel dimers through the interaction of the rod domains of two polypeptides, that forming stable tetramers or protofilaments leads to the formation of protofibrils [5].

GFAP, with microtubules and microfilaments, makes up the cytoskeleton of most eukaryotic cells and is the major IF in the adult brain and in mature astrocytes [6]. These cells are involved in a wide range of CNS pathologies, including trauma, ischemia and neurodegeneration [7–10]. Indeed, in response to any CNS pathology, astrocytes undergo a characteristic change in appearance with an increased production of IF proteins [6]. Diseases that show increased GFAP protein include Alzheimer's disease [9], scrapie [8] and Creutzfeld–Jacob disease [9]. The first described neurologic disease associated with GFAP mutations that results in a gain-of-function fashion is Alexander's disease [10]. This pathology is characterized by the presence of proteinaceous aggregates in astrocytes, known as Rosenthal fibers mainly composed of GFAP, αβ-crystallin, and the heat shock protein HSP-27 [11]. Three forms of AxD are recognized based on age of onset. The current view of how GFAP mutations cause AxD is based on a combination of events including the accumulation of GFAP and Rosenthal fibers with the sequestration of protein chaperones, and the activation of stress response. Consequently, attention for therapeutics is now focused on reducing the elevate level of GFAP as well as of Rosenthal fiber.

Interestingly, recent reports from our group showed that ceftriaxone (**Cef**, CAS number 104376-79-6, $C_{18}H_{16}N_8Na_2O_7S_3 \cdot 3.5H_2O$, Fig. 1), a safe and multi-potent β-lactam antibiotic able to overcome the blood–brain barrier [12], successfully eliminated the cellular toxic effects of misfolded mutated GFAP in a cellular model of Alexander's disease [13]. Moreover, clinical findings indicated that the chronic, cyclical intravenous administration of ceftriaxone in a patient with adult-onset Alexander's disease induced a positive clinical outcome [14], and a four-year-long extension of the trial with ceftriaxone in this patient showed that the progression of neurodegeneration was halted and/or reversed by ceftriaxone, with a significant improvement of the quality of life of the patient [15].

The neuroprotective activity of **Cef** has been also documented in many experimental models of cerebral ischemia, amyotrophic lateral sclerosis, Parkinson's disease, and epilepsy [16,17]. Purported mechanisms involved include the ability of **Cef** to increase the glutamate transporter subtype 1 (GLT-1) activity in astrocytes that are impaired in their GLT-1 expression, and the enhancement by this drug of the degradation of misfolded proteins through a still undetermined mechanism [15]. Notably, the possibility of a direct interaction of this molecule with GFAP as a mechanism to exert its effect has not been investigated remaining elusive. Recently, we demonstrated that **Cef** is able to interact with α-synuclein inhibiting the protein aggregation and to protect PC12 cells from the exposure to oxidopamine, also known as 6-hydroxydopamine (6-OHDA) [16]. Thus, the characterization of the interaction between ceftriaxone and GFAP is crucial for brain research, in order to elucidate at molecular level the inhibitory effect of ceftriaxone to GFAP protein involved in neurodegenerative diseases. In this study, we investigate the ability of ceftriaxone to interact with GFAP using both physicochemical techniques and computational methods. The same approaches were used to study the interaction of GFAP with phenytoin sodium (**PHT**, CAS number 630-93-3, $C_{15}H_{11}N_2NaO_2$), an old anticonvulsant drug used in the treatment of epilepsy [18], with well-known neuroprotective properties [19], which is also able to counteract and protect cells from the toxic effects of mutated GFAP in a cellular model of Alexander's disease (unpublished data). Synchrotron radiation circular dichroism (SRCD) spectroscopy has been used to obtain structural information about the GFAP-ligands interactions and the effect of **Cef** and **PHT** molecules on the protein photo and thermal stability. The high sensitivity of SRCD spectroscopy to sample perturbations enables the investigation of ligand-binding interaction that could not be attempted by any other technique in terms of speed, ease, and small amount of material required [20].

Computational methods allowed the identification of the relevant putative binding site of either **Cef** or **PHT** on the dimer structure of GFAP, permitting to rationalize the spectroscopic experimental results.

We have found that both **Cef** and **PHT** interacted with GFAP increasing the content of ordered structure as well as enhancing its photo and thermal stability. These results suggests that a direct action of **Cef** and **PHT** on GFAP stability might play a role in the therapeutic action of this molecule in halting and/or reversing the neurodegenerative processes associated with Alexander' disease. Moreover, these findings suggest that **PHT** might have a therapeutic role similar to ceftriaxone in Alexander's disease.

2. Materials and methods

2.1. Synchrotron radiation circular dichroism spectroscopy

Lyophilised w.t. GFAP from human brain was purchased from GenWay Biotech (Fig. S1 in Supporting Material). Ceftriaxone and phenytoin sodium were obtained from Sigma-Aldrich. GFAP was reconstituted with deionized water obtaining a carbonate buffer solution at concentration of 0.66 mg/ml. Ligand solutions (270 μM) were prepared in deionized water. Sample concentrations were determined by UV–Vis spectroscopy. SRCD spectra from 180 to 260 nm were collected at Diamond B23 beamline module end-station B using bandwidth = 1.1 nm, integration time of 1 s, 1 nm digital resolution, 39 nm/min scan speed. Spectra were measured using Suprasil cell (Hellma Ltd.) with 0.02 cm pathlength. Thermal stability was monitored in the 5–90 °C temperature range at 5 °C increments with 5 min equilibration time using Quantum Peltier temperature controller. Protein UV photo-denaturation was investigated measuring twenty consecutive repeated scans for each sample. SRCD spectra were processed and analyzed using CDApps software [21].

2.2. Docking and molecular dynamics simulations

The homology modeling procedure for GFAP Rod Domain was described in the Supporting Material. Starting ceftriaxone and diphenylhydantoin ligand geometries were built with Ghemical 2.99.2 [22], and energy minimized at molecular mechanics level first, using Tripos 5.2 force field parametrization [23], and then at AM1 semi-empirical level.

The AM1-EM ligand structures were fully optimized using GAMESS program [24] at the Hartree-Fock level with STO-3G basis set, followed by a single-point HF energy evaluation at the 6-31G* level to derive the partial atomic charges for the ligands by the RESP procedure [25].

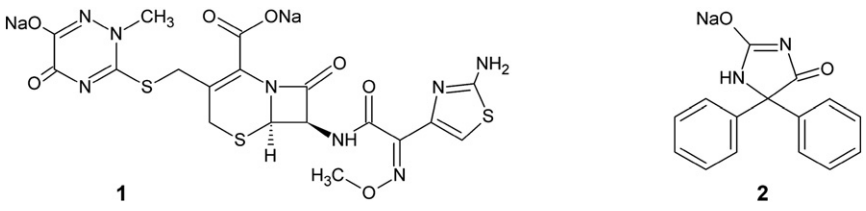

Fig. 1. Chemical structures of ceftriaxone sodium salt (**Cef**) (**1**) and phenytoin sodium (**PHT**) (**2**).

Docking studies were performed with AutoDock 4.2 [26] and AutoDockVina 1.1.2 [27]. The representative frames from MD simulations of each modeled GFAP region (see supporting material) and both ligands were processed with AutoDock Tools (ADT) package version 1.5.6rc1 [26] to merge non-polar hydrogens and calculate Gasteiger charges. Since potential ligand binding sites were unknown in advance, the whole modeled sequence of GFAP had to be targeted in docking. While the CC axes of the different GFAP fragments exhibit in general a locally variable curvature, both docking programs can only explore rectilinear boxes. Thus, to ensure a uniform sampling around the axis of each CC segment, sampling was performed on partially overlapping grids along the protein fragments, centered on "local sub-axis", (generated with the program AutoGrid 4.2 of Autodock 4.2 using 0.375 Å spacing and $100 \times 100 \times 100$ points), rather than a single grid encompassing the whole length of each CC segment and centered on the average segment axis. Hundred molecular AutoDock docking runs for each docking calculation were performed adopting a Lamarckian Genetic Algorithm (LGA) and the following associated parameters: 100 individuals in a population with a maximum of 15 million energy evaluations and a maximum of 37,000 generations were followed by 300 iterations of Solis and Wets local search. Flexibility was used for all rotatable bonds in both docked ligands. For each docking run from both Autodock and AutoDockVina, the poses with lowest predicted Autodock binding free energy within each highly-populated binding mode were selected for the subsequent molecular dynamics (MD) simulations of ligand-GFAP complexes.

For each ligand-protein complexes the addition of all hydrogen atoms, EM and MD simulations with Amber12 pmemd.cuda module [28,29] were carried out using ff12SB version of AMBER force field [30] for the protein and gaff parameters [31] for the ligands. MD simulation protocol was described in the supporting material.

2.3. Visual inspection, graphical analysis and structural Figs.

Visual inspection and graphical analysis were performed with VMD 1.9.2 [32] (also used to draw panels of Fig. M2) and UCSF Chimera 1.10.1 [33] (also used for panels of Figs. 7–10).

3. Results

3.1. Effects of Cef or PHT on the secondary structure of GFAP

The far-UV SRCD spectrum of GFAP in aqueous solution at 20 °C is characterized by the presence of a strong positive band at about 190 nm, and two negative bands at about 208 and 219 nm, diagnostic of the presence of an α-helical conformation component (Fig. 2). The addition of two equivalents of both ceftriaxone (**Cef**) and phenytoin (**PHT**), respectively, affected the far-UV SRCD spectrum of GFAP by increasing its CD intensity (Fig. 2 and Table 1). This unambiguously indicated that the both ligands bind to GFAP increasing its content of α-helical conformation by 14% and 16% respectively (Table 1).

3.2. Effects of Cef and PHT on both photo-induced and thermal GFAP denaturation

The protein stability of GFAP with and without ceftriaxone or phenytoin ligand was assessed with both UV photo and thermal denaturation assays.

The high UV photon flux of B23 beamline can denature proteins [35]. Indeed, a significant decrease of secondary structure upon light irradiation using intense far-UV radiations is well observable in structured proteins with significant content of α-helical and/or β-sheet conformations [36]. Like thermal denaturation, UV denaturation varies from protein to protein, and in the presence of ligands [20]. Protein denaturation induced by far UV radiation has been attributed to the formation of free radicals [37]. Previous studies using B23 beamline [28,38-42] has

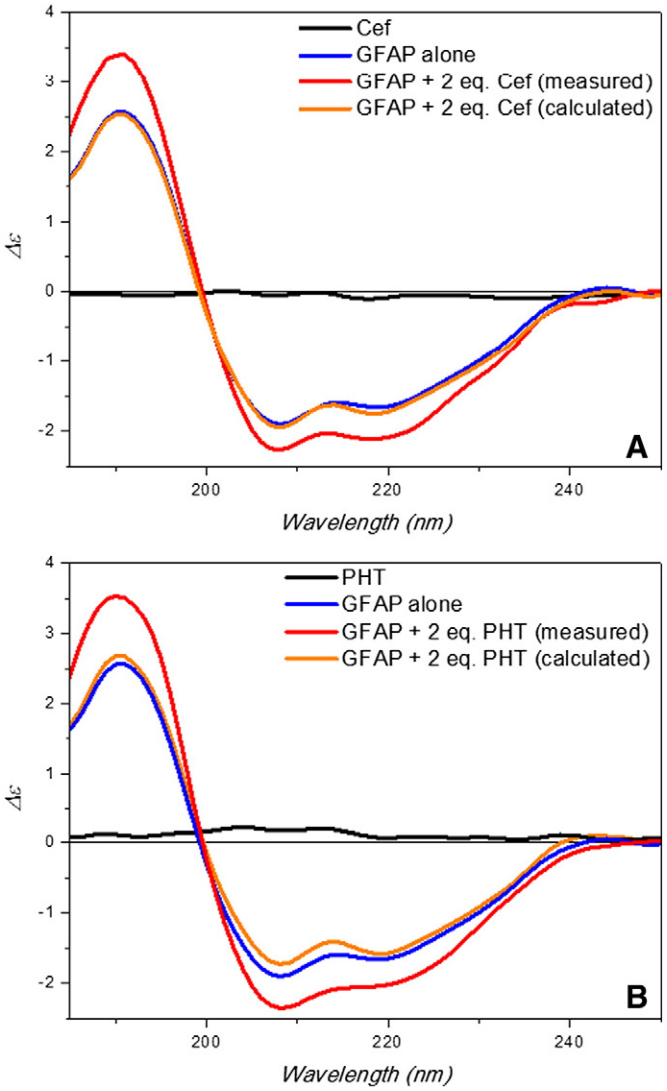

Fig. 2. Far-UV SRCD spectra of GFAP in aqueous solution in presence or absence of ceftriaxone (**A**) or phenytoin (**B**).

ruled out thermal stress from local heating induced by high photon flux in the far UV region. This was confirmed by different rates of conformation loss (denaturation) of the protein under heating and UV irradiation. The mechanism of photo-denaturation is likely to include free radical damage to the photosensitive residues tryptophan and tyrosine, as well as the oxidation of amino acid residue side chains [37,39–41]. Tyrosines are present in GFAP, which may explain the irreversible loss of conformation during UV irradiation. However, this phenomenon can be exploited as a protein UV-denaturation assay to assess the effect of the environment (solvent composition, detergents, pH, and ligands) on protein photo stability and specifically for ligand-protein binding interactions [20,36,39,42–46].

The UV-denaturation assay was carried out by measuring twenty consecutive repeated scans in the 180–250 nm far-UV region of aqueous GFAP with and without ceftriaxone (**Cef**) and phenytoin (**PHT**) (Fig. 3A, B and C). By keeping constant all the instrument parameters such as protein concentration, cell pathlength, volume of solution used to fill the cuvette cell, photon flux of the irradiating incident light that for the synchrotron beamline is characterized by the ring current value, the SRCD spectral changes were indicative of protein denaturation. This was better illustrated by the plot of SRCD intensity at single wavelength versus the number of scans. The fitting of the experimental data using 1st or 2nd order exponential equations (CDApps) can be seen as

Table 1
a-Helix content and thermodynamic properties of GFAP in presence or absence of ceftriaxone (**Cef**) or phenytoin (**PHT**) calculated using CONTINLL [34] of CDApps [21].

	Δε			% α-Helix	T_m (K)	ΔH (JM^{-1})	ΔS ($JK^{-1}\,M^{-1}$)
	190 nm	208 nm	219 nm				
GFAP	2.65	−1.95	−1.68	37	324.8 (51.8 °C)	91804	274.3
[b]GFAP + **Cef**	3.42	−2.31	−2.09	42 (>14%[a])	331.2 (58.2 °C)	68451	205
[b]GFAP + **PHT**	3.45	−2.37	−2.06	43 (>16%[a])	328.3 (55.3 °C)	148147	443

[a] The percentage is calculated from the ratio of α-helical percentage of the complex over that of GFAP.
[b] The value of α-helical content for the calculated GFAP + Cef and GFAP + PHT is similar to that of GFAP alone (37% α-helix).

the relative rates of UV-denaturation between GFAP with and without ceftriaxone and phenytoin ligands (Fig. 4A). Ceftriaxone appeared to increase the GFAP photo-stability much more than that induced by phenytoin. The rates of UV-denaturation of the GFAP complexes with **Cef** and **PHT** being different than that of GFAP were unambiguously indicative of ligand binding interactions. This was also consistent with the estimated amount of α-helical content from each of the 20 repeated consecutive SRCD scans that were different for GFAP + **Cef** and GFAP + **PHT** compared to that of GFAP (Fig. 4B). The one for GFAP + **PHT** appeared to be into two steps. However, the fact that the rates of UV-denaturation of the GFAP complexes were significantly different among themselves is an important observation, as this was not the case for the thermal denaturation studies where both complexes showed similar melting curves (Fig. 5B).

To confirm that the observed changes in the far-UV SRCD spectra of GFAP or complexed with the **Cef** and **PHT** ligands were not due to photo-induced protein fragmentation, electrophoresis of the irradiated samples were conducted showing that no new bands, in addition to those present in the starting material, were detected on the gel (Fig. S1) confirming the integrity of the protein in the first and last SRCD scans of the UV-denaturation assay experiments.

The temperature study of GFAP in the 5–90 °C temperature range revealed a partially reversible protein denaturation (Fig. 5A). On the contrary, in the presence of the two equivalents of ceftriaxone and phenytoin ligands the thermal denaturation of GFAP-ligands mixtures was more reversible than GFAP without ligands (data not shown). Both **Cef** and **PHT** ligands enhanced the thermal stability of GFAP (Fig. 5B) by increasing melting temperature T_m from 51.8 °C to 58.2 °C and 55.3 °C respectively (Table 1). Enthalpy of the complex with **Cef** (~68 kJM^{-1}) is much smaller than that of the complex with **PHT** (148 kJM^{-1}) suggesting that the complex with **PHT** is less favorable than the complex with **Cef**. This is also seen in the entropy of the complex with **Cef** (205 $JK^{-1}\,M^{-1}$) which is smaller than the complex with **PHT** (443 $JK^{-1}\,M^{-1}$), showing that the complex with **PHT** induces more disorder behavior of the complex while the presence of **Cef** induces more ordered structure to the complex compared to the GFAP alone (~92 kJM^{-1}) with entropy larger than the complex with **Cef**.

3.3. Homology modeling of GFAP predicted coiled-coil regions

GFAP (73–377), known as "rod" domain, exhibits the following predicted topologically organization (numberings in parenthesis correspond to the hGFAP sequence from UNIPROT: P14136): Coil 1A (73–104), Linker 1 (105–115), Coil 1B (116–214), Linker 1–2 (215–230), Coil 2A (231–252), Linker 2(253–256), Coil 2B (257–377). PSI-BLAST Similarity searches in the PDB dataset allowed the modeling of four dimeric CC region fragments, i.e. Coil 1A (73–104), Coil 1B (112–215), Coil 2A–2B (231–301) and Coil 2B (279–373), by using as templates the X-ray structures of Vimentin (PDB: 3G1E for Coil 1A, PDB: 3UF1 for 1B and PDB: 3TRT for 2A–2B) and Keratin (PDB: 3TNU for Coil 2B). Modeled regions share sequence identities of more than 60% with Vimentin template structures (Coil 1A: 75%, Coil 1B: 61%, Coil 2A–2B: 64%) and 42% with Keratin (Coil 2B).

Consistently with Vimentin structure, GFAP Coil 2A and 2B were modeled as a single continuous α-helical CC. GFAP Coil 2A–2B and Coil 2B have a short (22 aa) overlapping sequence. However, since we focused on possible binding modes of ceftriaxone and phenytoin to GFAP rather than on the structure of GFAP itself, we did not merged the two fragments, to facilitate the subsequent docking step.

The representative MD structures of each modeled GFAP CC region to be used in the subsequent docking calculations were obtained by a combined iterative fit and cluster analysis, described in "Methods" in the Supporting Material. Topological organization and CC motifs identified by SOCKET v. 3.02 [47] on the different representative modeled structures are illustrated in Fig. 6.

3.4. Molecular docking of Cef and PHT on GFAP

Docking calculations on **Cef** and **PHT** were performed with both Autodock [26] and AutoDockVina [27] programs, by a "multiple overlapping window" strategy, fully described in the "Methods" section, specifically devised for blind (i.e. on unknown binding site) docking on CC target structures. Briefly, docking was run for each compound in one to five (depending on the length of the modeled CC) consecutive and partially overlapping grid boxes for each GFAP fragment, to ensure a uniform distribution of sampled regions around the coil axes along all modeled fragments of GFAP, independently on the local CC curvature.

Both ligands exhibit an irregular distribution of the predicted binding poses for all CC segments, with 45 and 48 highly-populated "macrosites" for **Cef** and **PHT**, respectively (three for **Cef** and five for **PHT** in CC 1A, fourteen for **Cef** and eleven for **PHT** in 1B, ten for **Cef** and ten for **PHT** in 2A–2B, eighteen for **Cef** and twenty-two for **PHT** in 2B), corresponding to disjointed, multiply-populated blobs in Fig. 7.

3.5. MD refinement of selected complexes

The poses exhibiting most favorable predicted binding free energy in each highly-populated binding site were selected for MD simulation to assess the dynamic stability of the complexes.

The ligand-protein interaction energy, reported in Table S1 in the Supporting Material, along with the drift from the starting position and the time interval of stability, was calculated for poses that either were stable during a whole MD run, or rearranged to a new pose, stable for at least 6 ns of MD. For each ligand, only the structures within an energy cutoff of 40 kcal mol^{-1} from the absolute minimum of all complexes (bold energy values in Table S1) are discussed in detail in the subsequent sections. Hereafter "A" and "B" superscripts label residues from the model chains aligned with chains A or B of the corresponding PDB templates, respectively, while standard H-bonds, and H-bonds reinforced by ionic interactions are abbreviated as HB and HB-II, respectively. The protein residues involved in the main interactions with ligands for each selected complex model, discussed in the following section, are also reported in Table S2 in the Supporting Material.

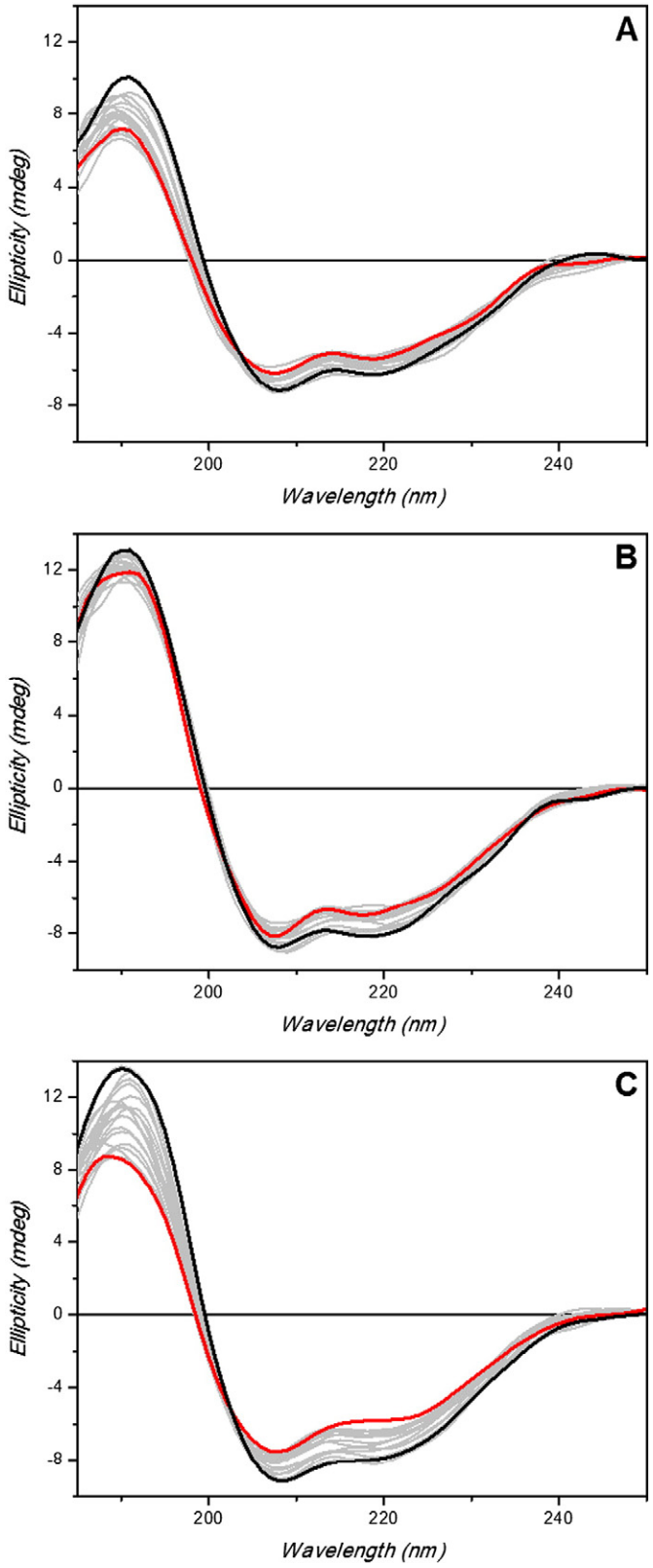

Fig. 3. GFAP UV-denaturation assay. **A**) Twenty repeated consecutive CD scans of GFAP (0.66 mg/ml) in aqueous solution measured with B23 module B. The solid black line indicates the first scan and the solid red line the 20th scan. Integration time 1 s, 0.02 cm cylindrical cell (30 μl), monochromator slit widths 0.500 mm (1.2 nm band width (bw)). **B**) Twenty repeated consecutive CD scans of GFAP-ceftriaxone (**Cef**) (1:2) complex in aqueous solution measured with B23 module B under the same experimental conditions. **C**) Twenty repeated consecutive CD scans of GFAP-phenytoin (**PHT**) (1:2) complex in aqueous solution measured with B23 module B under the same experimental conditions.

3.6. Complexes of Cef and PHT with Coil 1A

Five and three poses for **Cef** and **PHT**, named **Cef**/1A/1–5 and **PHT**/1A/1–3 (see Supporting Material for pose naming scheme), respectively, were selected from docking step and refined by MD runs of 10–25 ns (length depends on ligand rearrangement during MD). Stable poses for both ligands are highlighted in Table S1. In **Cef**/1A/4/md (Fig. 8B), **Cef** fits along the cleft between the two CC helices, forming with helix A a parallel-displaced π-stacking between its dioxotriazine ring and Phe89^{A} sidechain, HB-II with Lys86^{A} and HB between its amino group and Glu100^{A}, and with helix B a HB-II between the carboxylate group and Lys95^{B}. No **PHT**/1A complex exhibits an average interaction energy within the cutoff energy value, thus they will not be discussed in detail.

3.7. Complexes of Cef and PHT with Coil 1B

Due to the length of CC 1B, docking calculations were performed on five overlapping windows, i.e. w1 to w5, respectively providing five (**Cef**/1B/1–5), six (**Cef**/1B/6–11), four (**Cef**/1B/12–15), six (**Cef**/1B/16–21) and six (**Cef**/1B/22–26) poses for **Cef**, and four (**PHT**/1B/1–4), two (**PHT**/1B/5–6), two (**PHT**/1B/7–8), four (**PHT**/1B/9–12) and two (**PHT**/1B/13–14) poses for **PHT**, which were subsequently refined and assessed by MD runs of 10–30 ns, depending on the degree of pose rearrangement.

Among **Cef** complexes falling within the energy cutoff (**Cef**/1B/6, 9, 14, 19, 22) only in **Cef**/1B/22/md the ligand interacts with a single CC helix, whereas in the other poses it grafts the two CC helices together.

Ligand, in stable complexes, is located both toward the N-terminus (**Cef**/1B/6, 9/md), and in the middle (**Cef**/1B/14/d), and toward the C-terminus of the CC (**Cef**/1B/19, 22/md). Although in **Cef**/1B/6/md (Fig. 9C) **Cef** is mainly wrapped around helix A, it also forms strong HB-II interactions with Arg126^{B} on helix B, with both its dioxotriazine ring, and the carboxylate moiety. This latter, in turn, is also involved in HB-II with Arg124^{A}, thus bridging the two helices, turning a potential repulsive Arg-Arg inter-helical contact into a strong favorable Arg-carboxylate-Arg three-molecular interaction. The aminoimidazole group forms ionic-π interactions with Arg121^{A}. A similar binding mode occurs in **Cef**/1B/9/md (Fig. 9D) where the dioxotriazine ring fits between the two helices, forming HB-II with both Arg126^{A} and Arg124^{B}, while the aminothiazole ring engages a cation-π interaction with Arg136^{A}. In **Cef**/1B/14/d (Fig. 9E), **Cef** lies in the inter-helical cleft, forming a network of HB-II involving the aminothiazole ring and both Asp147^{A} and Arg162^{B}, dioxotriazine ring and Arg152^{B}, whereas the carboxylate group forms HB-II with Lys154^{A}. In **Cef**/1B/19/md (Fig. 9F), **Cef** is perpendicular to the CC axis and its dioxotriazine ring and carboxylate group engage cation-π and HB-II interactions, respectively, with Arg188^{A}. In addition, **Cef** amide carbonyl is H-bonded to Lys189^{A} and the aminothyazole group points toward Glu187^{B}, forming a low-persistence HBs during MD. In **Cef**/1B/22/md (Fig. 9G), **Cef** interacts mainly with a cluster of positively charged residues, i.e. Arg198^{A}, Arg201^{A} and Lys202^{A}, with both the dioxotriazine ring and the carboxylate moiety. It also forms hydrophobic interactions between its methoxymethyl group and Leu193^{B}/Glu196^{B}.

Among **PHT**/1B complexes, only **PHT**/1B/6/md (Fig. 9B) exhibited an average interaction energy within the cutoff. Here, **PHT** lies toward the N-terminus of CC and interacts with both helices, being its dioxoimidazolidine ring involved in a network of HBs and HB-II with Gln117^{B}, Arg121^{B} and Arg124^{B} on one helix and with Tyr116^{A}, on the other. This latter residue also forms π-stacking interactions with one **PHT** phenyl ring.

3.8. Complexes of Cef and PHT with Coil 2A-2B

Docking calculations of CC 2A–2B were performed on three overlapping windows, i.e. w1 to w3, respectively providing five (**Cef**/2A–2B/1–5), three (**Cef**/2A–2B/6–8) and six (**Cef**/2A–2B/9–14) poses for **Cef**, and

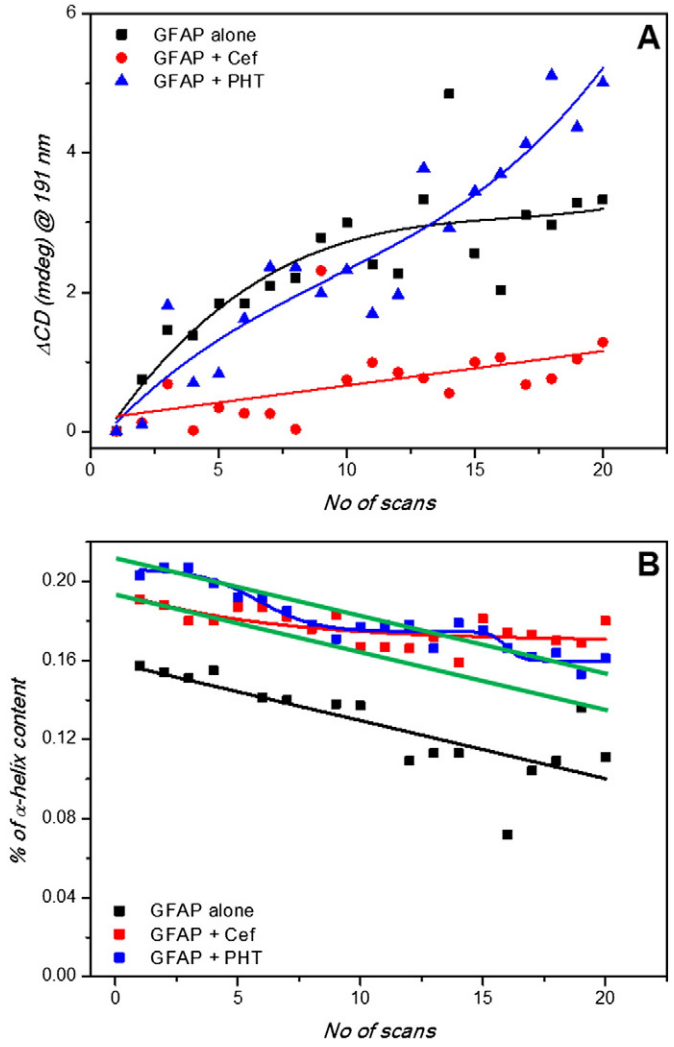

Fig. 4. SRCD intensity and secondary structure content versus the number of scans. **A**) Plot of the SRCD signal at 191 nm for GFAP (black), GFAP + **Cef** (1:2) (Red); and GFAP + **PHT** (1:2) (blue) versus number of scans. **B**) Plot of α-helix content for the GFAP (black), GFAP + **Cef** (1:2) (Red); and GFAP + **PHT** (1:2) (blue) determined with CONTINLL [34] of CDApps [21] from SRCD data versus number of scans. For all measurements GFAP concentration was 0.66 mg/ml, ligand concentration was 12 μM, protein/ligand ratio was 1:2. Ligands are ceftriaxone (**Cef**) and phenytoin sodium (**PHT**). The SRCD spectra (unsmoothed) were measured using B23 module B, integration time 1 s, 0.500 mm slit-width that corresponds to 1.2 nm bandwith using a cylindrical Suprasil cell of 0.02 cm pathlength (Hellma) filled with 30 μl of solution. The green lines are the shifted black line to illustrate the different slope of the red and blue lines.

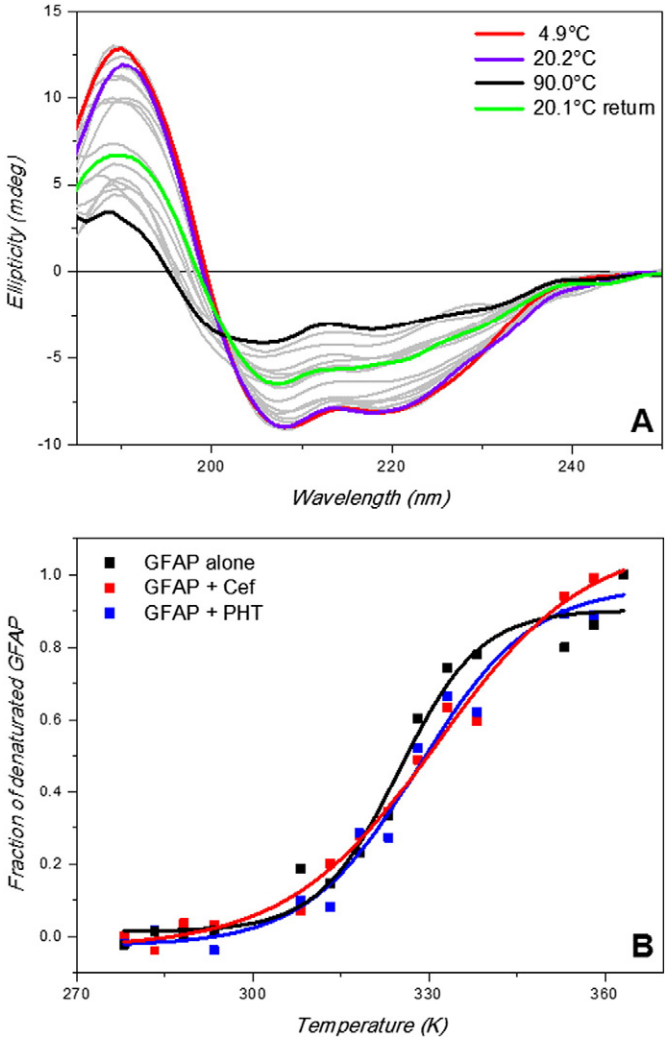

Fig. 5. GFAP thermal denaturation assay. A) Far-UV SRCD spectra of GFAP in aqueous solution measured with B23 module B at different temperatures. GFAP was 0.66 mg/ml; integration time 1 s, 0.02 cm cylindrical cell (30 μl), monochomator slit widths 0.280 mm (0.5 nm bandwidth) to eliminate the effect of UV denaturation. B) Plot of the fraction of denaturated protein calculated from the ellipticity values at 190 nm versus temperature. GFAP (black), GFAP + **Cef** (1:2) (Red); and GFAP + **PHT** (1:2) (blue).

two (**PHT**/2A–2B/1–2), two (**PHT**/2A–2B/4–5) and seven (**PHT**/2A–2B/6–12) poses for **PHT**, selected for MD refinement and assessment.

Among **Cef** poses that gave stable complexes only **Cef**/2A-2B/12, 13/md fell within the cutoff energy range. In both complexes, **Cef** is located at about 2/3 of the CC sequence. In **Cef**/2A–2B/12 (Fig. 10B), **Cef** is wrapped along helix B, engaging with its aminoimidazole ring both π-stacking and cation-π interaction with His281^{B} and Arg277^{B}, respectively. It also forms a bidentate HB-II between its carboxylate moiety and Lys280^{B}/Arg287^{B}. This latter residue also engages ionic interactions with dioxotriazine ring, which, in turn, forms HBs with Gln291^{B}. In **Cef**/2A–2B/13/md (Fig. 10C), instead, **Cef** molecule lies in the CC cleft, interacting with both helices by a network of HB-II and HBs involving its dioxotriazine ring and Arg271^{A}/Asn272^{A}, its carboxylate and carbonyl moieties and Lys280^{B} and its aminothiazole ring and Asn284^{B}, aminothiazole ring also engaging a cation-π interactions with Arg287^{B}.

Among **PHT** complexes, only **PHT**/2A–2B/9/md (Fig. 10D) showed average energy-interaction very close to the cutoff. **PHT** is located toward the C-terminal end of CC and mainly interacts with helix A: the dioxoimidazolidine moiety forms a network of HBs with Ser292^{A}, Gln289^{A} and HB-II with Arg288^{A}, whereas a phenyl group engages hydrophobic interactions with both Leu293^{A} and Leu290^{B}.

3.9. Complexes of Cef and PHT with Coil 2B

Docking calculations on CC 2B were run on five overlapping windows, i.e. w1 to w5, respectively providing the following selected poses for the MD assessment: three (**Cef**/2B/1–3), three (**Cef**/2B/4–6), seven (**Cef**/2B/7–13), six (**Cef**/2B/14–20) and eight (**Cef**/2B/21–27) poses for **Cef**, and four (**PHT**/2B/1–4), three (**PHT**/2B/5–7), eight (**PHT**/2B/8–15), four (**PHT**/2B/16–19) and five (**PHT**/2B/20–23) poses for **PHT**. Among the stable **Cef** poses, only **Cef**/2B/2/md (Fig. 10H) exhibited an average energy value within the cutoff. The ligand is located toward the N-terminus of the protein, perpendicularly to the CC axis and spanning both the helices: the dioxotriazine ring and the carboxylate group engage HBs with Gln291^{B} and HB-II with Arg287^{B}, respectively, whereas the aminoimidazole ring and the carbonyl group of amidic moiety form HBs with Asp296^{A} and Gln291^{A}, respectively. Among **PHT** complexes, two of them, i.e. **PHT**/2B/2/md (Fig. 10F) and **PHT**/2B/3/md (Fig. 10G) fell within the energy cutoff, sharing a very similar binding

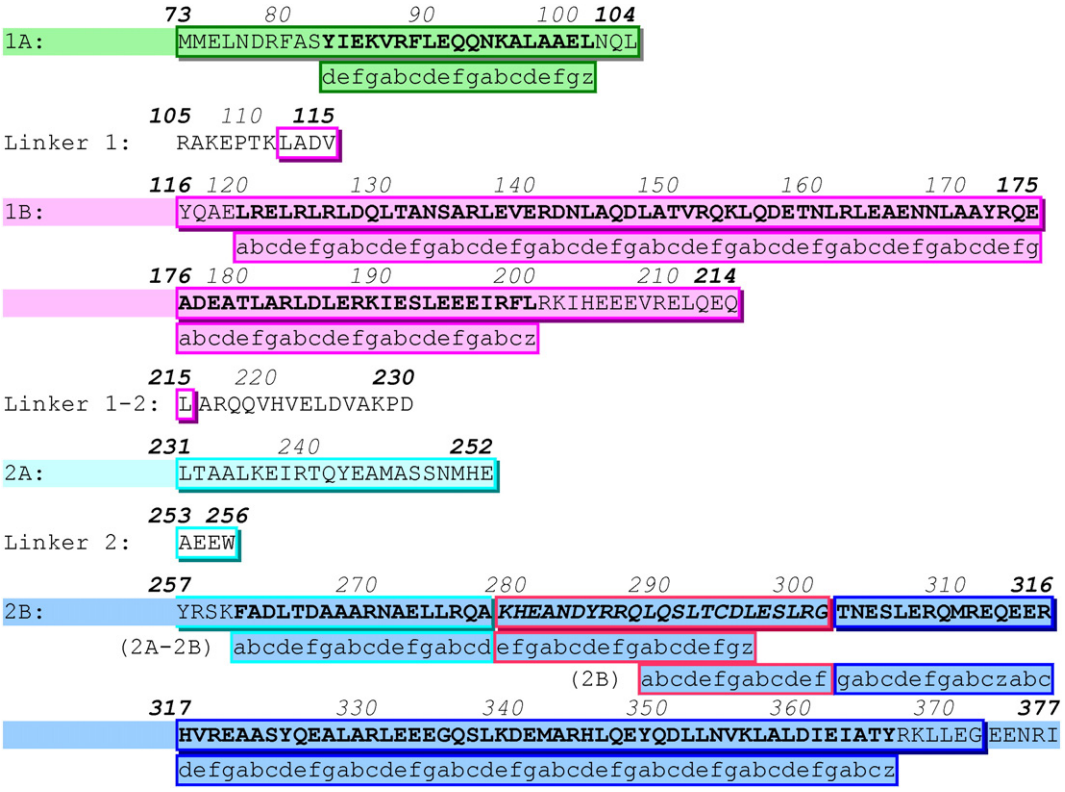

Fig. 6. Annotated sequence of hGFAP rod domain. hGFAP(73–377) from UNIPROT: P14136 is shown with: predicted topological elements listed on the left and, for coils 1A, 1B, 2A and 2B, also highlighted with light green, magenta, cyan, blue background, respectively; modeled regions enclosed in shadowed boxes; CC motifs identified by SOCKET v. 3.02 [46] in the representative models in bold (1A = 19aa; 1B = 86aa; 2A–2B = 35aa; 2B = 78aa, with the corresponding heptad (abcdefg) assignment one row below); model 2A–2B/2B overlapping region boxed in red. SOCKET assignments for both 2A–2B and 2B segments (consistently labeled in parentheses) are shown under the first row of the coil 2B sequence.

mode: the ligand is positioned toward the N-terminus of the protein, mainly interacting with only one helix of CC. Its dioxoimidazoline ring forms a network of HB-II and HBs with $Arg287^{A}$, $Arg288^{A}$ (both poses) and $Gln291^{A}$ (only **PHT**/2B/2/md), while one phenyl ring engages hydrophobic interactions with $Leu290^{A}$ and, in **PHT**/2B/2/md only, the other forms a π-stacking with $Tyr285^{B}$, the only relevant interaction with the second CC chain.

3.10. Influence of complexation on protein local structural stability

To evaluate the effects of the different complexes on the structural stability of protein segments, an analysis (Table S2) of protein backbone atom rmsd focused on "local" (i.e. around the binding site of each ligand) interactions, as described in detail in "Methods", was performed on the final set of structures highlighted in Table S1. This "local" approach gets rid of possible noise from both long timescale "breathing" motions of the segments (under sampled on the simulated timescales) and instant to medium timescale random fluctuations, especially affecting the terminal regions of the segments and potentially amplified by their elongated shape.

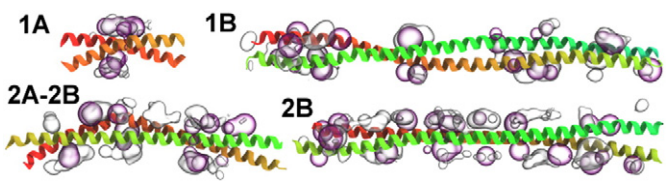

Fig. 7. Distribution of **Cef** and **PHT** docking poses for different GFAP segments. Transparent surfaces (violet: **Cef**, light gray: **PHT**) enclose docked ligand centers of selected poses in all the complexes with GFAP (**1A**), (**1B**), (**2A**–**2B**) and (**2B**). GFAP segments are represented by ribbons colored by an "absolute-scale, per-protein rainbow" scheme, ranging from red (N-terminus of the A chain) to cyan (C-terminus of the B chain of the longest, i.e. 1B, sequence), and accordingly narrower scales for shorter segments.

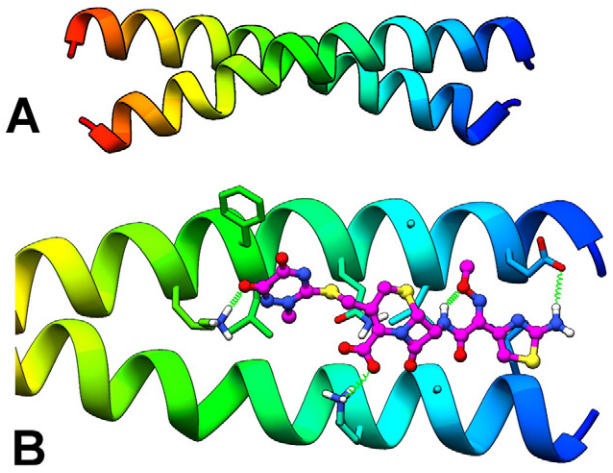

Fig. 8. Structure of the 1A modeled protein segment and of the corresponding selected complexes with **Cef** or **PHT**. The representative structure of the 1A (**A**) GFAP segment is shown in ribbon representation, with a "relative-scale, per-chain rainbow" coloring scheme, ranging from red (N-terminus) to blue (C-terminus) for each chain of each sequence. Panel (**B**) shows the binding regions of the selected 1A complex: **Cef**/1A/4/md. Protein ribbons and sidechain carbon atoms are colored as in (**A**). **Cef** is shown in ball-and-stick representation, with carbon atoms colored in magenta. Protein sidechains within 5 Å from ligands are shown as sticks. Protein-ligand H-bonds are represented as green "springs". Nitrogen, oxygen, sulfur, hydrogen atoms are colored blue, red, yellow and white, respectively.

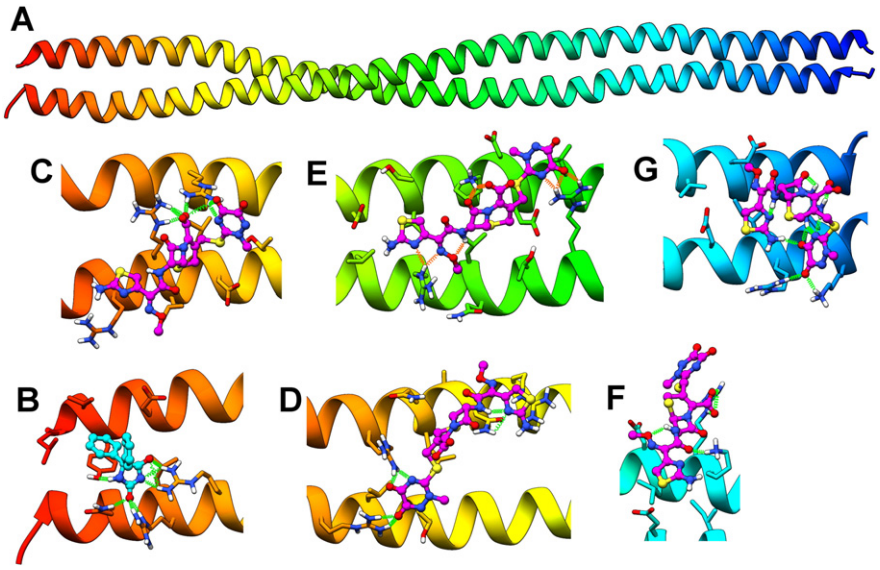

Fig. 9. Structure of the 1B modeled protein segment and of the corresponding selected complexes with **Cef** or **PHT**. The representative structure of the 1B GFAP segment (**A**) and the binding regions of selected 1B complexes: **PHT**/1B/6/md (**B**), **Cef**/1B/6/md (**C**) **Cef**/1B/9/md (**D**), **Cef**/1B/14/d (**E**), **Cef**/1B/19/md (**F**) and **Cef**/1B/22/md (**G**), are shown using the same representations and coloring schemes described in Fig. 8.

4. Discussion

In previous work, we documented that a chronic, cyclical treatment with **Cef** in a patient with adult-onset Alexander's disease halted, and partly reversed, the progression of neurodegeneration [14,15]. Recently, we found that ceftriaxone interacts with α-synuclein and inhibits its pathological aggregation [16], suggesting the possibility of a chaperone-like effect of this molecule on protein involved in specific neurodegenerative diseases [48]. These findings prompted us to evaluate the occurrence of a direct effect of ceftriaxone on GFAP.

We have demonstrated that GFAP stability was increased by the binding interactions with **Cef** (Figs. 4 and 5B). SRCD spectra showed that the addition of **Cef** increased the content of α-helical structure on native hGFAP, increased the protein melting temperature T_M and reduced the UV photo denaturation (Figs. 4 and 5B). Similarly, **PHT**, an antiepileptic drug with definite neuroprotective activity [19], which is also able to counteract the toxic effects of mutated GFAP in a cellular model of Alexander's disease (unpublished data), interacted directly with GFAP increasing even more the content of α-helical conformation than that with Cef (Table 1). On the other hand, **PHT** resulted to be less efficient to protect GFAP toward UV and thermal denaturation (Figs. 4 and 5B).

In order to understand how **Cef** and **PHT** interact with GFAP, we conducted computational studies to predict the potential binding sites

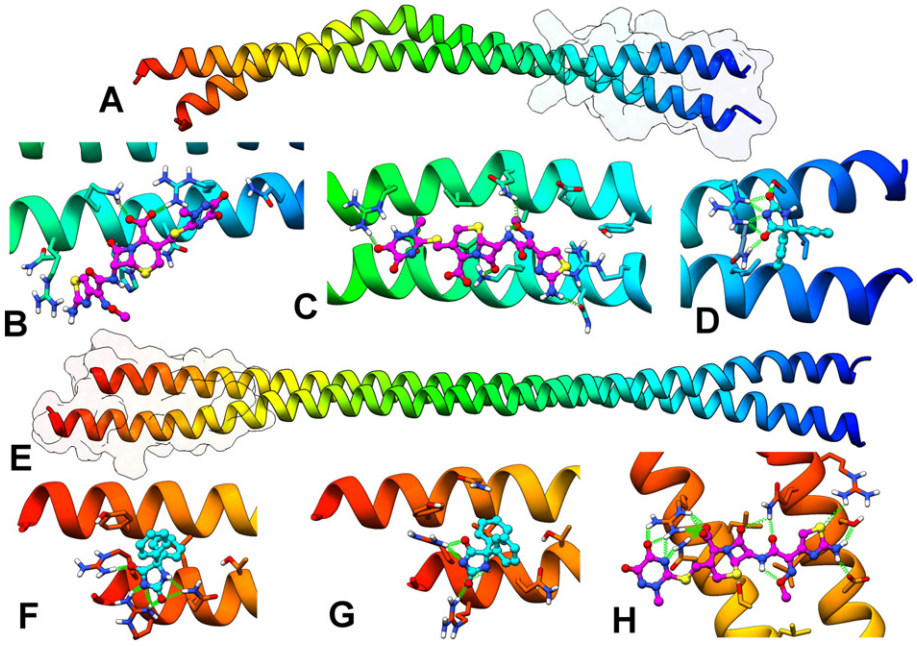

Fig. 10. Structure of the 2A-2B and 2B modeled protein segments and of the corresponding selected complexes with **Cef** or **PHT**. The representative structures of the 2A–2B (**A**) and 2B (**E**) and the binding regions of selected 2A–2B (**B**–**D**) and 2B (**F**–**H**) complexes: **Cef**/2A–2B/12/md (**B**), **Cef**/2A–2B/13/md (**C**), **PHT**/2A–2B/9/md (**D**), **PHT**/2B/2/md (**F**), **PHT**/2B/3/md (**G**) and **Cef**/2B/2/md (**H**), are shown using the same representations and coloring schemes described in Fig. 8.

of **Cef** and **PHT** to GFAP. The preliminary modeling of GFAP segments provided structures exhibiting a considerable conformational stability on the 10^1 ns timescale simulated for their MD refinement.

Modeling of GFAP complexes with **Cef** and **PHT** shows that both ligands can form non-covalent complexes stable on a $>10^1$ ns timescale. However, the lack of a canonical "binding site", intended as a more or less deep concavity, like those observed in most receptor or enzyme active sites, implies that both the nature of the binding, and its strength cannot be evaluated with the usual standards and protocols of more canonical complex examples. In particular, MD identified four main classes of dynamic behaviors of the ligands: 1) "labile", in which the interaction predicted by docking is lost during the MD and the ligand moves away from the protein, 2) "traveling", where ligand loses its starting protein interactions during the MD, but it moves on the protein surface, always preserving some direct contact with it; 3) "rearranging", in which the ligand moves away from its starting position, but it reaches within few ns a new pose, stable for at least 6 ns, until the end of the simulations; 4) "stable", where the ligand remains in the starting pose during the whole MD simulation. In particular, the occurrence of "traveling" and "rearranging" complexes, in addition to the aforementioned lack of deep binding sites, is also favored by the high occurrence of similar, repeating patterns of hydrophobic and charged (especially basic) residues along a considerable fraction of the modeled CC sequences.

The only partial exception to the lack of a binding cavity is represented by the (quite shallow, indeed) clefts between CC helices and parallel to CC axis: in this view it is not surprising that the only observed low-energy "stable" pose, **Cef**/1B/14/d, exhibits the ligand in an inter-helical cleft, lying parallel to the CC axis.

Since the nature of the complexes and their high dynamic ranges make the quantitative evaluation of ligand affinities an even more than usually elusive task, we will only discuss emerging qualitative and macroscopic quantitative features of the different complexes and ligands.

The comparison between the two ligands shows that **Cef** provides a larger number of low energy and persistent poses than **PHT** (nine vs. four with our computational approach and a 40 kcal mol^{-1} cutoff on the protein-ligand interaction energy). This behavior is consistent with SRCD results showing that **PHT** is less efficient in protecting GFAP against UV- and thermal denaturation. The ligand distribution along the protein segments exhibits low energy poses in all modeled sequences for **Cef**, with a peak in the 1B CC, where five out of the nine low energy and persistent poses are found. However, when the standard topological organization is considered, we must observe that no selected complex involves the 2A CC region, since all the selected poses in 2A–2B model dock toward the C-terminus, i.e. in the 2B part, in a sequence that overlaps the 2B segment N-terminus, exhibiting a very similar binding mode to the best complexes selected for this latter region. In the case of **PHT**, ligand is observed in low energy and persistent poses only in 1B (one pose) and in the overlapping 2B region corresponding to the C-terminus of 2A–2B and the N-terminus of 2B sequences (three poses).

When considering the possible implication of the predicted ligand binding on overall tertiary and quaternary structure of GFAP, although we cannot exclude effects deriving from eventual interactions of the ligands with regions of GFAP that could not be modeled, some possible effects of binding on protein structure can be predicted from our models.

In principle, the binding of a ligand on a CC can affect the stability of the coil and of the single intervening helices either negatively, by disrupting or altering a pattern of sidechain–sidechain, or even sidechain–backbone/backbone–backbone interactions, strongly contributing to the stability of both structures, or positively, by aspecific patching of apolar patches on the protein surface, or by specific protein-ligand stabilizing interactions.

A comparison of the local rmsd fluctuations of the protein backbone atoms between free and complexed protein MD simulations (Table S2), shows that the stability of helices and CCs, although already very good in the MD models of unligated segments (see "Homology Modeling of GFAP predicted coiled-coil regions"), is generally improved upon binding of **Cef**, and, to a lesser extent, **PHT**. In particular, is considerable (>15%) in seven of the selected poses (six for **Cef** and one for **PHT**), significant (about 8%) in two poses (one for **Cef** and one for **PHT**), and marginal (<5%) in the other four selected poses (two for **Cef** and two for **PHT**). In this view, an overall net stabilization of the helical structure upon binding is expected for the two ligands, especially in ligand concentration ranges where multiple-binding states are significantly populated. This stabilization is fully consistent with the increase in helicity suggested by SRCD results in the presence of **Cef** and **PHT** (Table 1).

However, when comparing their binding modes, a different behavior between the two ligands is observed. **Cef** appears to bind preferentially to canonical CC conformations that are all located in regions identified by SOCKET v. 3.02 belonging to CC motifs, except for three residues out of 36 listed in the table ($Arg201^A$ and $Lys202^A$ for **Cef**/1B/22/md and $Arg287^B$ for **Cef**/2B/2/md) that are within two residues of the ends of the corresponding CC motifs. **PHT**, on the other hand, appears to prefer the less-regular regions at both ends of canonical CC motifs as three out of 17 listed residues lies outside the canonical + two-adjacent-residue region. Only one out of the four selected models (**PHT**/2 A-2B/9/md) interacts with residues within canonical CC motifs. This behavior can be attributed to the relatively small size of **PHT**, which is unable to full "clamp" either a single helix or, even more, a CC helix pair, and thus can form stable complexes by lying in the cleft between two interacting helices. However, since the cleft formed by canonical CC motifs is quite narrow and very shallow, it represents a good binding site only when its considerable length can be fully exploited by a properly-sized and shaped ligand, like for **Cef** in the following complexes: **Cef**/1A/4/md (Fig. 8B), **Cef**/1B/14/d (Fig. 9E) and **Cef**/2A–2B/13/md (Fig. 10C). In this view, the wider inter-helical clefts located in regions immediately surrounding the canonical CC motifs provide a better binding site for a ligand of the size and shape of **PHT**. Overall, **Cef** and **PHT** appear to stabilize prevalently CC structures by different mechanisms; **Cef** by stabilizing the CC motif itself by clamping the two helices together and/or enforcing their interactions and covering their surfaces along the inter-helical cleft; **PHT** by locking potentially flexible hinge regions flanking canonical CC motifs.

5. Conclusions

This study determined the binding of **Cef** and **PHT** drugs to hGFAP by SRCD spectroscopy and examined how these ligands might interact with predicted coil-coiled regions of the hGFAP protein by molecular docking and dynamics. We observed that both these molecules interact directly with GFAP increasing the content of α-helical structure. UV and thermal denaturation assays revealed that GFAP exhibited enhanced stability upon the addition of two equivalents of each ligands with **Cef** imparting a more spontaneous interactions than **PHT** and more ordered complex system than **PHT**. GFAP-ligand complexes in particular with higher ligand stoichiometry either by high ligand concentration and/or affinity could prevent the formation of larger protein aggregates by capping possible local oligomerization regions. At the same time, by changing/altering the nature of exposed chemical groups on the protein surface could create a potentially disturbing factor for the building up of specific networks for polar interactions. Also at higher concentrations, the dynamic of less defined and weaker "traveling" protein-ligand interactions observed for several MD models could provide aspecific extra stabilization of helical regions and/or destabilization of further protein aggregation.

This effect is more evident by the addition of **Cef**, suggesting a stronger protective effect of this molecule, in neurological disorders characterized by an increased production and polymerization of GFAP.

Conflict of interest

The authors declare no competing financial interest.

Transparency document

The Transparency document associated with this article can be found, in the online version.

Acknowledgment

We thank Diamond Light Source for access to beamline B23 (SM8034) that contributed to the results presented here. The research leading to these results has received funding from the European Community's Seventh Framework Program (FP7/2007–2013) under grant agreement no. 226716.

Appendix A. Supplementary data

Supplementary data to this article can be found online at http://dx.doi.org/10.1016/j.bbagen.2016.04.021.

References

[1] D. Dahl, D.C. Rueger, A. Bignami, K. Weber, M. Osborn, Vimentin, the 57 000 molecular weight protein of fibroblast filaments, is the major cytoskeletal component in immature glia, Eur. J. Cell Biol. 24 (1981) 191–196.
[2] S.E. Boyd, B. Nair, S.W. Ng, J.M. Keith, J.M. Orian, Computational characterization of 3′ splice variants in the GFAP isoform family, PLoS One 7 (2012).
[3] J.E. Ralton, X. Lu, A.M. Hutcheson, R.A. Quinlan, Identification of 2 n-terminal non-alpha-helical domain motifs important in the assembly of glial fibrillary acidic protein, J. Cell Sci. 107 (1994) 1935–1948.
[4] T.C. Savidge, M.V. Sofroniew, M. Neunlist, Starring roles for astroglia in barrier pathologies of gut and brain, Lab. Investig. 87 (2007) 731–736.
[5] E. Fuchs, K. Weber, Intermediate filaments — structure, dynamics, function, and disease, Annu. Rev. Biochem. 63 (1994) 345–382.
[6] J. Middeldorp, E.M. Hol, GFAP in health and disease, Prog. Neurobiol. 93 (2011) 421–443.
[7] C. Kaur, V. Sivakumar, Y. Zhang, E.A. Ling, Hypoxia-induced astrocytic reaction and increased vascular permeability in the rat cerebellum, Glia 54 (2006) 826–839.
[8] H. Gomi, T. Yokoyama, S. Itohara, Role of GFAP in morphological retention and distribution of reactive astrocytes induced by scrapie encephalopathy in mice, Brain Res. 1312 (2010) 156–167.
[9] S. Jesse, P. Steinacker, L. Cepek, C.A.F. von Arnim, H. Tumani, S. Lehnert, H.A. Kretzschmar, M. Baier, M. Otto, Glial fibrillary acidic protein and protein S-100B: different concentration pattern of glial proteins in cerebrospinal fluid of patients with Alzheimer's disease and Creutzfeldt–Jakob disease, J. Alzheimers Dis. 17 (2009) 541–551.
[10] T. Yoshida, M. Nakagawa, Clinical aspects and pathology of Alexander disease, and morphological and functional alteration of astrocytes induced by GFAP mutation, Neuropathology 32 (2012) 440–446.
[11] R. Nau, H.W. Prange, P. Muth, G. Mahr, S. Menck, H. Kolenda, F. Sorgel, Passage of cefotaxime and ceftriaxone into cerebrospinal-fluid of patients with uninflamed meninges, Antimicrob. Agents Chemother. 37 (1993) 1518–1524.
[12] T. Bachetti, E. Di Zanni, P. Balbi, P. Bocca, I. Prigione, G.A. Deiana, A. Rezzani, I. Ceccherini, G. Sechi, In vitro treatments with ceftriaxone promote elimination of mutant glial fibrillary acidic protein and transcription down-regulation, Exp. Cell Res. 316 (2010) 2152–2165.
[13] W. Rosenthal, Über eine eigenthümliche, mit Sylingomyelie complicirte Geschwulst des Ruckenmarks, Beitr. Pathol. Anat. 23 (1898) 111–143.
[14] G. Sechi, M. Matta, G.A. Deiana, P. Balbi, T. Bachetti, E. Di Zanni, I. Ceccherini, A. Serra, Ceftriaxone has a therapeutic role in Alexander disease, Prog. Neuro-Psychopharmacol. Biol. Psychiatry 34 (2010) 416–417.
[15] G. Sechi, I. Ceccherini, T. Bachetti, G.A. Deiana, E. Sechi, P. Balbi, Ceftriaxone for Alexander's disease: a four-year follow-up, JIMD Rep. 9 (2013) 67–71.
[16] P. Ruzza, G. Siligardi, R. Hussain, A. Marchiani, M. Islami, L. Bubacco, G. Delogu, D. Fabbri, M.A. Dettori, M. Sechi, N. Pala, Y. Spissu, R. Migheli, P.A. Serra, G. Sechi, Ceftriaxone blocks the polymerization of alpha-synuclein and exerts neuroprotective effects in vitro, ACS Chem. Neurosci. 5 (2014) 30–38.
[17] T.C.H. Leung, C.N.P. Lui, L.W. Chen, W.H. Yung, Y.S. Chan, K.K.L. Yung, Ceftriaxone ameliorates motor deficits and protects dopaminergic neurons in 6-hydroxydopamine-lesioned rats, ACS Chem. Neurosci. 3 (2012) 22–30.
[18] M.M. Goldenberg, Overview of drugs used for epilepsy and seizures: etiology, diagnosis, and treatment, Pharm. Ther. 35 (2010) 392–415.
[19] L.J. Willmore, Antiepileptic drugs and neuroprotection: current status and future roles, Epilepsy Behav. 7 (2005) S25–S28.
[20] R. Hussain, T. Jávorfi, G. Siligardi, B.23 spectroscopic analysis: synchrotron radiation circular dichroism, in: E.M. Carreira, H. Yamamoto (Eds.), Comprehensive Chirality, Elsevier, Amsterdam 2012, pp. 438–448.
[21] R. Hussain, K. Benning, D. Myatt, T. Jávorfi, E. Longo, T.R. Rudd, B. Pulford, G. Siligardi, CDApps: integrated software for experimental planning and data processing at beamline B23 Diamond Light Source, J. Synchrotron Radiat. 22 (2015) 465–468.
[22] T. Hassinen, M. Peräkylä, New energy terms for reduced protein models implemented in an off-lattice force field, J. Comput. Chem. 22 (2001) 1229–1242.
[23] M. Clark, R.D. Cramer, N. Van Opdenbosch, Validation of the general purpose tripos 5.2 force field, J. Comput. Chem. 10 (1989) 982–1012.
[24] M.W. Schmidt, K.K. Baldridge, J.A. Boatz, S.T. Elbert, M.S. Gordon, J.H. Jensen, S. Koseki, N. Matsunaga, K.A. Nguyen, S.J. Su, T.L. Windus, M. Dupuis, J.A. Montgomery, General atomic and molecular electronic-structure system, J. Comput. Chem. 14 (1993) 1347–1363.
[25] T. Fox, P.A. Kollman, Application of the RESP methodology in the parametrization of organic solvents, J. Phys. Chem. B 102 (1998) 8070–8079.
[26] G.M. Morris, R. Huey, W. Lindstrom, M.F. Sanner, R.K. Belew, D.S. Goodsell, A.J. Olson, AutoDock4 and AutoDockTools4: automated docking with selective receptor flexibility, J. Comput. Chem. 30 (2009) 2785–2791.
[27] O. Trott, A.J. Olson, Software news and update AutoDock Vina: improving the speed and accuracy of docking with a new scoring function, efficient optimization, and multithreading, J. Comput. Chem. 31 (2010) 455–461.
[28] A.W. Götz, M.J. Williamson, D. Xu, D. Poole, S. Le Grand, R.C. Walker, Routine microsecond molecular dynamics simulations with AMBER on GPUs. 1. Generalized born, J. Chem. Theory Comput. 8 (2012) 1542–1555.
[29] R. Salomon-Ferrer, A.W. Götz, D. Poole, S. Le Grand, R.C. Walker, Routine microsecond molecular dynamics simulations with AMBER on GPUs. 2. Explicit solvent particle mesh Ewald, J. Chem. Theory Comput. 9 (2013) 3878–3888.
[30] D.A. Case, T.A. Darden, T.E. Cheatham III, C.L. Simmerling, J. Wang, R.E. Duke, et al., AMBER 12, University of California, San Francisco, 2012 (http://ambermd.org/doc12/Amber12.pdf).
[31] J. Wang, R.M. Wolf, J.W. Caldwell, P.A. Kollman, D.A. Case, Development and testing of a general amber force field, J. Comput. Chem. 25 (2004) 1157–1174.
[32] W. Humphrey, A. Dalke, K. Schulten, VMD: visual molecular dynamics, J. Mol. Graph. 14 (1996) 33–38.
[33] E.F. Pettersen, T.D. Goddard, C.C. Huang, G.S. Couch, D.M. Greenblatt, E.C. Meng, et al., UCSF chimera—a visualization system for exploratory research and analysis, J. Comput. Chem. 25 (2004) 1605–1612.
[34] S.W. Provencher, J. Glockner, Estimation of globular protein secondary structure from circular dichroism, Biochemistry 20 (1981) 33–37.
[35] D.T. Clarke, G. Jones, CD12: a new high flux beamline for ultraviolet and vacuum-ultraviolet xxcircular dichroism on the SRS Daresbury, J. Synchrotron Radiat. 11 (2004) 142–149.
[36] R. Hussain, T. Javorfi, G. Siligardi, Circular dichroism beamline B23 at the Diamond Light Source, J. Synchrotron Radiat. 19 (2012) 132–135.
[37] A.J. Grosvenor, J.D. Morton, J.M. Dyer, Profiling of residue-level photo-oxidative damage in peptides, Amino Acids 39 (2010) 285–296.
[38] T. Jávorfi, R. Hussain, D. Myatt, G. Siligardi, Measuring circular dichroism in a capillary cell using the B23 synchrotron radiation CD beamline at Diamond Light Source, Chirality 22 (2010) E149–E153.
[39] E. Longo, R. Hussain, G. Siligardi, Application of circular dichroism and magnetic circular dichroism for assessing biopharmaceuticals formulations photo-stability and small ligands binding properties, Int. J. Pharm. 480 (2015) 84–91.
[40] E. Longo, E. De Santis, R. Hussain, C. van Der Walle, J. Casas-Finet, S. Uddin, A. dos Santos, G. Siligardi, The effect of palmitoylation on the conformation and physical stability of a model peptide hormone, Int. J. Pharm. 472 (2014) 156–164.
[41] G.H. Xu, M.R. Chance, Hydroxyl radical-mediated modification of proteins as probes for structural proteomics, Chem. Rev. 107 (2007) 3514–3543.
[42] D. Lörinczy, Effect of nucleotides and environmental factors on the intermediate states of ATP hydrolysis cycle in skeletal muscle fiinte, in: D. Lörinczy (Ed.), The Nature of Biological Systems as Revealed by Thermal Methods, Springer 2004, pp. 159–186.
[43] G. Siligardi, R. Hussain, CD spectroscopy: an essential tool for quality control of protein folding, in: R.J. Owens (Ed.), Structural Proteomics: High-Throughput Methods, Methods in Molecular Biology, vol. 1261 2015, pp. 255–276.
[44] S.R. Martin, M.J. Schilstra, G. Siligardi, Circular Dichroism, in: A. Podjarmy, A. Dejaegere, B. Kieffer (Eds.), Biophysical Approaches Determining Ligand Binding to Biomolecular Targets, Detection, Measurement and Modelling, RSC Publishing 2011, pp. 226–246.
[45] G. Siligardi, R. Hussain, Biomolecules interactions and competitions by non-immobilised ligand interaction assay by circular dichroism, Enantiomer 3 (1998) 77–87.
[46] G. Siligardi, B. Panaretou, P. Meyer, S. Singh, D.N. Woolfson, P.W. Piper, L.H. Pearl, C. Prodromou, Regulation of Hsp90 ATPase activity by the co-chaperone Cdc37p/p50^{cdc37}, J. Biol. Chem. 277 (2002) 20151–20159.
[47] J. Walshaw, D.N. Woolfson, SOCKET: a program for identifying and analysing coiled-coil motifs within protein structures, J. Mol. Biol. 307 (2001) 1427–1450.
[48] G. Sechi, P. Balbi, T. Bachetti, I. Ceccherini, Safe drugs to fight mutant protein overload and alpha-1-antitrypsin deficiency, J. Hepatol. 55 (2011) 949–950.